Diagnostics and two-dimensional simulation of low-frequency inductively coupled plasmas with neutral gas heating and electron heat fluxes

K. N. Ostrikov, I. B. Denysenko, E. L. Tsakadze, S. Xu, and R. G. Storer

Related Articles

Additional information on J. Appl. Phys.

Diagnostics and two-dimensional simulation of low-frequency inductively coupled plasmas with neutral gas heating and electron heat fluxes

K. N. Ostrikov[a]
*Plasma Sources and Applications Center, NIE, Nanyang Technological University, 1 Nanyang Walk,
637616 Singapore and School of Chemistry, Physics and Earth Sciences, The Flinders University of South
Australia, Adelaide SA 5001, Australia*

I. B. Denysenko
*Plasma Sources and Applications Center, NIE, Nanyang Technological University, 1 Nanyang Walk,
637616 Singapore and School of Physics and Technology, Kharkiv National University, 4 Svobody sq.,
61077 Kharkiv, Ukraine*

E. L. Tsakadze
*Plasma Sources and Applications Center, NIE, Nanyang Technological University, 1 Nanyang Walk,
637616 Singapore and Optics and Fluid Dynamics Department, RISOE National Laboratory, P.O. Box 49,
DK-4000 Roskilde, Denmark*

S. Xu[b]
*Plasma Sources and Applications Center, NIE, Nanyang Technological University, 1 Nanyang Walk,
637616 Singapore*

R. G. Storer
*School of Chemistry, Physics and Earth Sciences, The Flinders University of South Australia,
Adelaide SA 5001, Australia*

This article presents the results on the diagnostics and numerical modeling of low-frequency ($\sim$460 KHz) inductively coupled plasmas generated in a cylindrical metal chamber by an external flat spiral coil. Experimental data on the electron number densities and temperatures, electron energy distribution functions, and optical emission intensities of the abundant plasma species in low/intermediate pressure argon discharges are included. The spatial profiles of the plasma density, electron temperature, and excited argon species are computed, for different rf powers and working gas pressures, using the two-dimensional fluid approach. The model allows one to achieve a reasonable agreement between the computed and experimental data. The effect of the neutral gas temperature on the plasma parameters is also investigated. It is shown that neutral gas heating (at rf powers$\geq$0.55 kW) is one of the key factors that control the electron number density and temperature. The dependence of the average rf power loss, per electron–ion pair created, on the working gas pressure shows that the electron heat flux to the walls appears to be a critical factor in the total power loss in the discharge. © *2002 American Institute of Physics.*
[DOI: 10.1063/1.1510598]

I. INTRODUCTION

In recent years, there has been a steadily growing interest in the "fine engineering" of low-temperature plasmas for numerous high-tech applications in low-temperature plasma-enhanced synthesis of nanocomposite and biocompatible materials, nanoscale assemblies, ultra-fine etching, patterning and microstructuring of semiconductor wafers in ultralarge scale integration large-scale manufacturing, micromachining, development of active elements in photonic devices, and many others.[1] The fine engineering concept involves the development of sophisticated means of generating the plasma to comply with the specific requirements, and controlling the plasma species composition, number densities and fluxes towards surfaces being processed.[2,3] In particular, the common requirements for the suitability of low-temperature plasmas for most high-tech applications are high uniformity of ions and active neutral species over the discharge cross section and volume, high product yield with low damage, process selectivity, and reproducibility.[4,5] Sources of inductively coupled plasmas (ICPs) with external flat spiral coils[6] do meet the above requirements and as such are widely adopted by the semiconductor industry as reference plasma reactors for microelectronic circuitry fabrication.

In applications, the operating conditions of ICPs can vary over broad ranges, e.g., the plasma needs to remain fairly stable when the gas feedstock pressure varies from a few mTorr to a few atmospheres. However, low-pressure operating regimes still remain favorable for most of the existing applications of ICPs. It is remarkable that the rf power transfer efficiency in low-pressure ICP devices is usually very high thus making it possible to generate dense ($n_i \sim 8$

[a]Also with: Division of Microelectronics, School of Electrical and Electronic Engineering, Nanyang Technological University, 639798 Singapore.
[b]Author to whom correspondence should be addressed; electronic mail: syxu@nie.edu.sg

$\times 10^{11}$–8×10^{12} cm^{-3}, where n_i is the ion density) plasmas with moderate rf input powers.[4,6–8]

Most of the existing modeling and experimental efforts are focused on 13.56 MHz inductively coupled plasmas, widely used nowadays by the semiconductor and other industries. However, sources of lower frequency rf plasmas are gaining rapidly increasing attention due to a number of indisputable advantages. In particular, operating ICP devices with frequencies in the range 0.46–0.5 MHz has proved unexpectedly efficient in producing highly uniform, high-density plasmas in large volumes.[9–16] Moreover, low-frequency rf plasma devices have great potential for upscaling[9,10] and for controlling the electron energy distribution functions (EEDFs),[16] rates of the major gas-phase reactions,[17] optical emission intensity, and mode transition thresholds,[15] as well as various thin film deposition[14] and nanoassembly[18] processes. This certainly makes the sources of low frequency ICPs (LF ICPs) attractive as prototypes of large-volume commercial plasma reactors.

To date, most modeling studies of the electromagnetic effects and particle/power balance in ICPs have been made using either the fluid model[19–22] or the particle-in-cell method[23,24] with Monte Carlo collisions,[25] or hybrid models.[26] The nonlocal kinetic approach[27] can also be used to simulate the plasma parameters at low gas pressures. It is remarkable that, despite relative modeling simplicity, the fluid models appear to be able to resolve much of the relevant physics with reasonable accuracy within a tolerable computational cost.[28]

Most recently, it has been recognized that heating of the neutral gas in low-temperature ICP sources during plasma processing can result in notable distortions of the uniformity of the neutral number densities across the chamber leading to variations of the plasma parameters, composition, temperatures, and number densities of the reactive species, as well as chemical reaction rates.[29] Similarly, gas heating strongly affects the discharge electrodynamics and particle kinetics in microwave surface wave sustained plasmas.[30,31]

Here, we aim at incorporating the neutral gas heating effects into the two-dimensional (2D) fluid simulation of low-frequency ICPs and verify the model experimentally using Langmuir probe and optical emission spectroscopy (OES) techniques. Thus, the key internal discharge parameters, such as the plasma density, electron temperature, and EEDF are examined by Langmuir probe diagnostics. The high-resolution OES technique is used to study the optical emission intensity (OEI) of the abundant plasma species in different ranges of the working gas pressure. The modeling work is based on an improved 2D fluid model for an argon plasma, accounting for the heating of the neutral gas and the electron heat flux to the walls. The computed electron/ion number densities, electron temperatures, and optical emission intensities of the excited argon species appear to be consistent with the experimentally measured values. The dependence of the average power loss per an electron–ion pair created on the working gas pressure is studied as well.

The paper is organized as follows. In Sec. II, we describe the experimental setup, ancillary equipment, and diagnostic tools. The basic assumptions, equations and boundary condi-
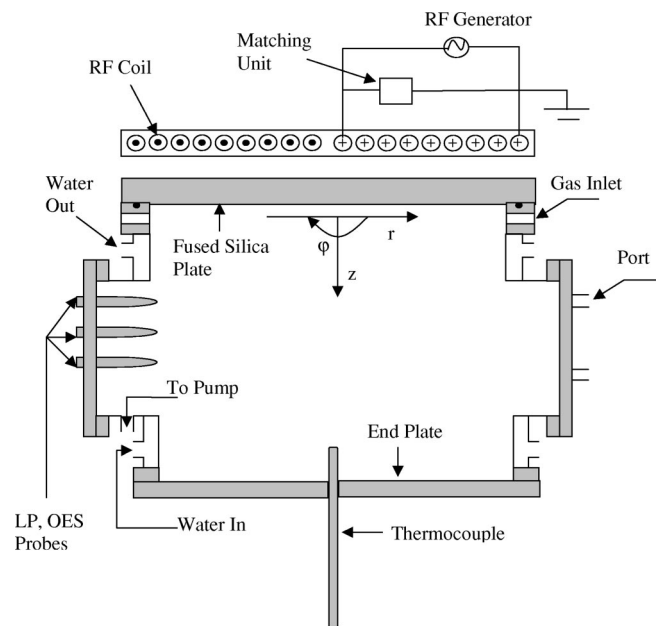

FIG. 1. Schematic diagram of the discharge chamber.

tions of the 2D model are presented in Sec. III. In Sec. IV, the profiles of the plasma parameters are computed for different rf powers, working gas pressures and temperatures and compared with the results of the Langmuir probe measurements. A satisfactory agreement between the results of optical emission spectroscopy and the computed OEI profiles is also reported. The results obtained and pathways for further improvement of the model and experimental techniques are discussed in Sec. V. A brief summary of this work and the outlook for future research are given in the Conclusion, Sec. VI.

II. EXPERIMENTAL DETAILS

Experimental measurements have been carried out in the low-frequency ($\sim$0.46 MHz) inductively coupled plasma source described in detail elsewhere.[12,15] The plasma is generated in a cylindrical, stainless steel vacuum chamber with inner diameter $2R=32$ cm and length $L=20$ cm (Fig. 1). The chamber is cooled by a continuous water flow in between the inner and outer walls of the chamber. The top plate of the chamber is a fused silica disk, 35 cm in diameter and 1.2 cm thick. A 450 l/s turbomolecular pump backed by a two-stage rotary pump is used to evacuate the plasma chamber. The inflow rate and pressure of the working gas are regulated by a combination of a gate valve and MKS mass-flow controllers. The pressure is measured by an MKS Baratron capacitance manometer. The operating pressure of argon gas feedstock is typically maintained in the range $p_0 = 20$–200 mTorr. The global plasma parameters, such as the electron/ion number densities, plasma potential and effective electron temperature have been estimated by means of a time-resolved rf-compensated single Langmuir probe technique. The electron energy distribution function has been calculated using the Dryuvestein routine employing the second derivative of the Langmuir probe current-voltage characteristics.[5] A number of holes in four rectangular side

ports and in the bottom plate of the chamber allow one to insert the Langmuir probe into the plasma and move it in radial and axial directions. The optical emission from the ICP discharge has been collected using a light receiver mounted on different port holes and transmitted via the optical fiber to a SpectroPro-750 spectrometer (Acton Research Corporation) with the resolution of 0.023 nm. The OES of excited neutral and/or ionized argon atoms have been investigated in the wavelength range 350–850 nm. Further details of the Langmuir probe and optical emission intensity measurements can be found elsewhere.[12,15] Due to the limited space of the article, the experimental results are presented in the computation sections to enable a direct comparison.

III. MODEL DESCRIPTION

A. Basic assumptions

Theoretically, the plasma chamber is modeled by considering a metal cylinder of the inner radius R and length L, with a dielectric disk of width d and permittivity ϵ_d atop. The components of the electromagnetic field are calculated assuming that the chamber is uniformly filled by the plasma with the electron/ion number density equal to the spatially averaged plasma density $\bar{n}$.

The main results of this article are relevant to the pressure range 20–100 mTorr, where the contribution of nonlocal collisionless heating is usually smaller than that of collisional heating.[32] Our model of the rf power deposition is thus solely based on the assumption of the prevailing ohmic (collisional) heating.

To simulate the real environments of some of the plasma processing experiments[14] the study is carried out for elevated rf powers absorbed in a plasma column $P_{in} = 0.6$–1.4 kW. Consequently, the density of electrons is large, and the electron–electron collisions are expected to strongly affect the EEDFs.

B. Electromagnetic fields

The components of the transverse-electric (TE) electromagnetic field in the chamber fully filled by the uniform plasma with the plasma density $\bar{n}$ are

$$B_z^p = A \sum_{n=1}^{\infty} \frac{\alpha_{1n} \kappa_n^H}{D_n(\text{TE})} \zeta_n^H(z) J_0(\kappa_n^H r), \tag{1}$$

$$B_r^p = A \sum_{n=1}^{\infty} \frac{\alpha_{1n} \gamma_n^H}{D_n(\text{TE})} \eta_n^H(z) J_1(\kappa_n^H r), \tag{2}$$

and

$$E_\phi^p = i \frac{\omega}{c} A \sum_{n=1}^{\infty} \frac{\alpha_{1n}}{D_n(\text{TE})} \zeta_n^H(z) J_1(\kappa_n^H r), \tag{3}$$

where

$$\zeta_n^H(z) = \sinh[\gamma_n^H(L-z)]/\cosh(\Gamma_n^H d)\cosh(\gamma_n^H L),$$

$$\eta_n^H(z) = \cosh[\gamma_n^H(L-z)]/\cosh(\Gamma_n^H d)\cosh(\gamma_n^H L),$$

$$D_n(\text{TE}) = \Gamma_n^H \coth(\Gamma_n^H d) + \gamma_n^H \coth(\gamma_n^H L),$$

$$\alpha_{1n} = [8\pi/cR^2 J_2^2(\rho_{1n})] \int_0^R r J_1(\kappa_n r) dr,$$

where ϕ is the azimuthal angle, $\Gamma_n^H = [(\kappa_n^H)^2 - (\omega/c)^2 \varepsilon_d]^{1/2}$ and $\gamma_n^H = [(\kappa_n^H)^2 - (\omega/c)^2 \varepsilon_p]^{1/2}$ are the inverse rf field penetration lengths into dielectric and plasma, respectively.[12] Furthermore, we have $J_j(x)$ is a Bessel function of the jth order, $J_1(\rho_{1n}) = 0$, $\kappa_n^H = \rho_{1n}/R$, $\varepsilon_p = 1 - \omega_{pe}^2/[\omega(\omega + i\nu_{en})]$ is the dielectric constant of the uniform plasma and $\omega_{pe} = \sqrt{4\pi\bar{n}e^2/m_e}$ is the electron Langmuir frequency. Here, ν_{en} is the electron–neutral collision frequency for momentum transfer, A is a constant, and e and m_e are electron charge and mass, respectively.

The averaged plasma density is computed from the particle and power balance equations (see the following subsection) and substituted into the electromagnetic fields Eqs. (1)–(3), which are continuously updated when $\bar{n}$ varies.

C. Particle and power balance

Since the column and inductive coils are fairly uniform in azimuthal direction, the problem is two dimensional and the plasma parameters depend on r and z only. It is assumed that the ion temperature T_i is equal to the temperature of the working gas T_g. The latter was a variable parameter in the computations. The plasma is treated within the ambipolar model that assumes the plasma quasineutrality and the equality of electron and ion fluxes. The effect of negative ions is neglected so that the overall charge neutrality condition can be written as $n_e = n_i \equiv n$, where n_e is the electron number density.

Accordingly, the particle balance equation for the electrons or ions is

$$\partial n/\partial t + \boldsymbol{\nabla} \cdot (n\mathbf{v}) = n\nu^i, \tag{4}$$

where $\mathbf{v}$ is the electron or ion fluid velocity, and ν^i is the ionization rate. We recall that in the ambipolar diffusion-controlled regime[5]

$$\mathbf{v} \approx -\nabla(nT_e)/nm_i\nu_{in},$$

where $\nu_{in} \approx \sqrt{v^2 + v_{Ti}^2}/\lambda$ is the ion–neutral collision frequency, m_i is the ion mass, and $T_i \ll T_e$. Here, $\lambda = 1/(n_N\sigma_{in})$ is the ion mean free path, where we have used $\sigma_{in} = 8 \times 10^{-15}$ cm^2, $v_{Ti} = \sqrt{8T_i/\pi m_i}$ is the average ion thermal velocity, and $n_N = p_0/T_g$ is the number density of neutrals, and T_e is the electron temperature. We note that in computation T_e was self-consistently derived from the set of electrodynamic, plasma particle and rf power balance equations. On the other hand, in the experiment, T_e was measured through the averaged electron energy $\langle \mathcal{E} \rangle$ as $T_e = 2/3 \langle \mathcal{E} \rangle$, as required by the Dryuvestein's routine.[5]

The rf power balance in the discharge is described by[33]

$$\frac{3}{2} n_e \frac{\partial T_e}{\partial t} + \boldsymbol{\nabla} \cdot \mathbf{q}_e \approx -n_e I_e + S_{ext}, \tag{5}$$

where I_e is the collision integral for the electrons, and $\mathbf{q}_e \approx -(5/2 - g_u)n_e T_e/(m_e\nu_{en})\boldsymbol{\nabla}T_e$ is the heat flux density with $g_u = (T_e/\nu_{en})\partial\nu_{en}/\partial T_e$. The term S_{ext} denotes the Joule heating of the electrons by the rf field

$$S_{\text{ext}} \approx n\nu_e m_e u_{\text{osc}}^2,$$

where $u_{\text{osc}} \approx |eE_\phi^p|/[2m_e^2(\omega^2 + \nu_{\text{en}}^2)]^{1/2}$ is the time-averaged oscillation velocity of the electrons in the rf field. The equilibrium state corresponds to setting $\partial_t = 0$ in Eqs. (4) and (5). Our approach is valid for fixed rf power absorption in the plasma column, with

$$P_{\text{in}} = \int_0^L \int_0^R S_{\text{ext}} 2\pi r \, dr \, dz,$$

which also yields the constant A in Eqs. (1)–(3). The rate of the electron–neutral collisions ν_{en} that depends on T_e has been determined using the elastic scattering rate coefficients.[20]

Assuming that the excitation and ionization of the neutral gas goes mainly via the electron impact processes, one infers that the collision integral I_e is equal to the average power lost by an electron colliding with a neutral. Accordingly,

$$I_e \approx (3m_e/m_n)T_e\nu_{\text{en}} + \sum_j \nu_j \mathcal{E}_j + \nu^i \mathcal{E}^i,$$

where m_n is the mass of the neutral, ν_j is the excitation rate from the ground state to level j with a threshold energy $\mathcal{E}_j$, and $\mathcal{E}^i$ is the ionization threshold energy. Stepwise ionization and excitation processes are not accounted in the present simulation.

For argon gas, the rates for ionization and excitation to the states $4s$ and $4p$ are[34]

$$\nu^i = 2.3n_N \times 10^{-8} T_e^{0.68} \exp(-\mathcal{E}_i/T_e) \ s^{-1},$$

$$\nu_{4s} = 5.0n_N \times 10^{-9} T_e^{0.74} \exp(-\mathcal{E}_{4s}/T_e) \ s^{-1},$$

and

$$\nu_{4p} = 1.4n_N \times 10^{-8} T_e^{0.71} \exp(-\mathcal{E}_{4p}/T_e) \ s^{-1},$$

where n_N is in cm^{-3}, T_e in eV, $\mathcal{E}_i = 15.76$ eV, $\mathcal{E}_{4s} = 11.5$ eV, and $\mathcal{E}_{4p} = 13.2$ eV. It is notable that the above rate coefficients were calculated by assuming the EEDFs Maxwellian.[34]

We now consider the boundary conditions for integrating Eqs. (4)–(5). Because of symmetry, the radial gradients of the electron temperature and density are equal to zero at the chamber axis ($r=0$). At the column edge ($r=R$) the radial component of the fluid velocity satisfies the well-known Bohm sheath criterion $v_r(R,z) = \sqrt{T_e(R,z)/m_i}$.[5] Similarly, at the side walls $z=z_s$, where $z_s = 0$ or L, we have $v_z(r,z_s) = \sqrt{T_e(r,z_s)/m_i}$. Likewise, the boundary conditions for heat flow are[33]

$$q_{\text{er}}(R,z) = T_e(R,z)(2 + \ln\sqrt{m_i/m_e})$$
$$\times n(R,z)\sqrt{T_e(R,z)/m_i}, \tag{6}$$

and

$$q_{\text{ez}}(r,z_s) = T_e(r,z_s)(2 + \ln\sqrt{m_i/m_e})$$
$$\times n(r,z_s)\sqrt{T_e(r,z_s)/m_i}, \tag{7}$$

where q_{er} and q_{ez} are the radial and axial components of the heat flux density, respectively.
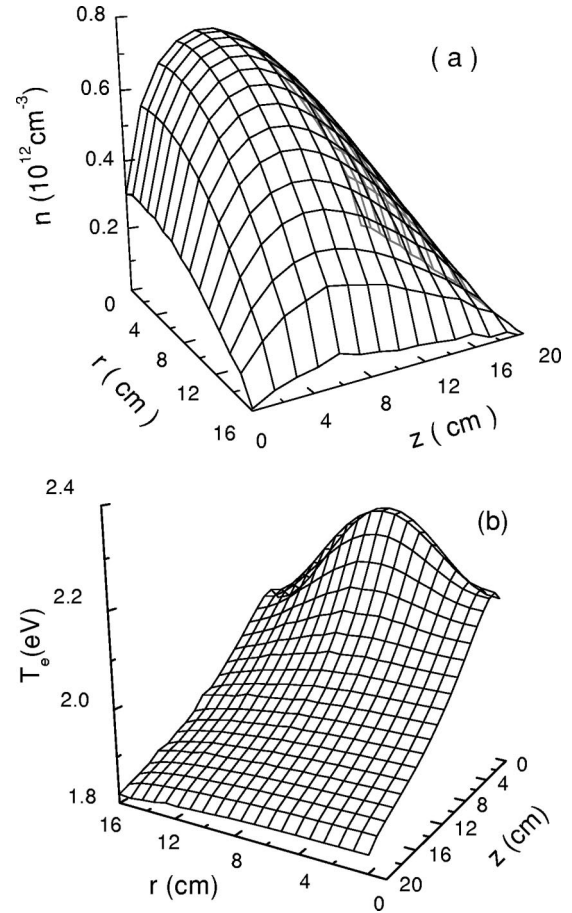

FIG. 2. Numerical profiles of the plasma density (a) and electron temperature (b) at $p_0 = 28.5$ mTorr, $P_{\text{in}} = 612.4$ W, and $T_g = 543$ K.

The set of Eqs. (4)–(5) has been solved numerically. The details of the codes and numerical procedures can be found elsewhere.[35,36] The profiles of the electron density, temperature and ion velocity are computed from Eqs. (4)–(5). The resulting electron density distribution is used to compute the spatially averaged plasma density $\bar{n}$. Thereafter, the latter is substituted into Eq. (3) to obtain the azimuthal electric field $E_\phi^p(r,z)$. The computation is initialized using profiles of n, $\mathbf{v}$, and T_e estimated from less accurate analytical or computational results. The computation goes through a number of temporal steps and is terminated when a steady state is reached.

IV. NUMERICAL AND EXPERIMENTAL RESULTS

A. Effect of rf power

We now report on the spatial profiles of the electron number density and temperature in the LF ICP obtained numerically using the 2D fluid model and experimentally using the Langmuir probe technique.

The calculated 2D profiles of the electron number density and temperature at $p_0 = 28.5$ mTorr and $P_{\text{in}} = 612.4$ W are shown in Fig. 2. One can see that the electron temperature is maximal near chamber top at $r \approx 8$ cm. The profile of T_e is linked to the spatial distribution of E_ϕ^p (3). Since the electron temperature is somehow elevated near the fused
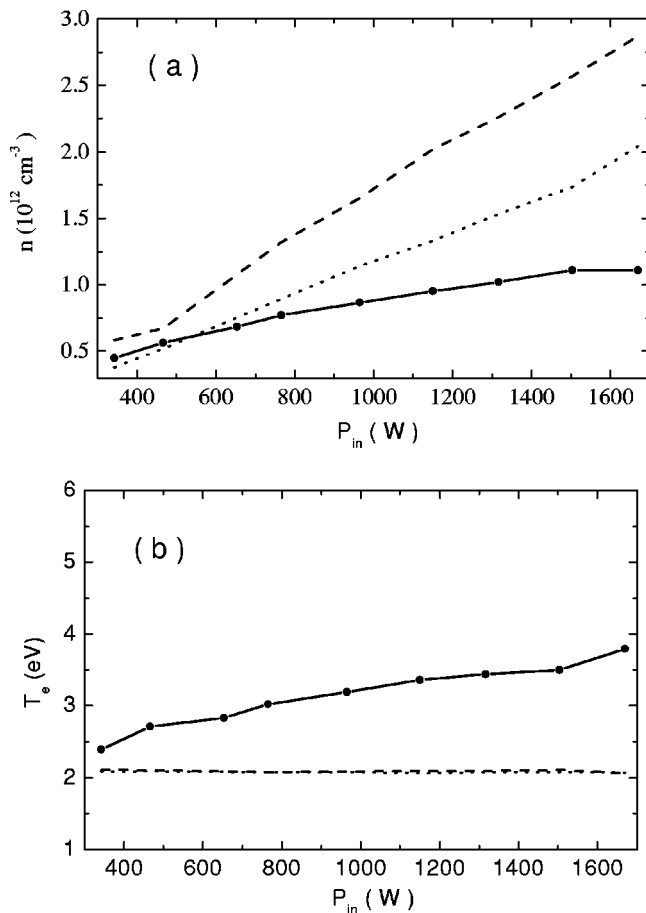
FIG. 3. The computed and measured electron density (a) and temperature (b) at axial $z = 5.6$ cm, and radial $r = 4$ cm positions in the chamber. The circles correspond to the experimental data. Dotted and dashed curves are calculated for the boundary condition for the heat flux (i) and (ii), respectively. Other parameters are the same as in Fig. 2.

silica window, the maximum of the plasma density is shifted approximately 3 cm upwards ($z \approx 7$ cm) from the central cross section of the chamber center ($z_0 = 10$ cm). We note that in the classical case of uniform distribution of T_e, over the entire chamber, one would expect a cosine-like solutions for the plasma density, with the maximum at $z = z_0$.[5]

The computed electron number densities and temperatures have been compared with the ones measured by the Langmuir probe, with the tip positioned at $z = 5.6$ cm and $r = 4.0$ cm. Figure 3 displays the computed and measured values of n_e and T_e as functions of the input rf power P_{in}. The computation has been carried out under two different boundary conditions for the electron heat flux:

(i)   the electron heat flux towards the boundary is governed by Eqs. (6) and (7); and

(ii)   the electron temperature gradient vanishes at the boundary ($\nabla T_e = 0$). This boundary condition has been commonly used in simulations alongside with Eqs. (6) and (7).[19,33]

From Fig. 3(a) one can see that the plasma density obtained using boundary conditions (i) is closer to the experimentally measured one. Indeed, for nonvanishing heat flux boundary conditions (i), in the rf power range of P_{in}

< 800 W the computed plasma density almost fully recovers the experimental data [Fig. 3(a)]. As the power increases ($P_{in} > 800$ W), the simulation yields plasma densities somewhat higher than the measured ones. The discrepancy can possibly be attributed to consistent elevation of the electron temperature at higher power levels [solid lines with circles in Fig. 3(b)], which cannot be reflected by the ambipolar-diffusion particle loss model adopted in our simulation [dashed and dotted curves in Fig. 3(b)], where a power-independent value of T_e is normally the case.[5] It is thus natural to expect that the particle loss in the discharge in question transit to other, than the ambipolar-diffusion controlled, mode, with higher T_e (and hence, thermal motion power loss), and lower n_e at fixed rf power levels. Further evidence and discussion on the possible particle loss mode conversion follows in Sec. IV B.

We emphasize that the best agreement with the experiment is achieved by carefully accounting for nonvanishing electron heat fluxes, thus making the boundary conditions (i) more appropriate for modeling inductively coupled plasmas at elevated powers. Specifically, application of (ii) instead of (i) would lead to higher values of the electron number density. Physically, the electron heat fluxes are capable of removing a part of the rf power, that could have otherwise been gainfully used for additional electron-ion pairs creation in the plasma bulk.

Variations of rf power apparently affect the distribution of the electromagnetic fields, which is depicted in Fig. 4. In Figs. 4(a) and 4(b) the axial and radial profiles of the computed electric field E_ϕ^p are shown for different values of the input power. One can see from Fig. 4 that the electric field increases near the chamber top and decreases more rapidly in the z direction when the input power rises. This is consistent with the well-known dependence of the rf field penetration length on the plasma density.[32] It is notable that at $z > 5$ cm the field component E_ϕ^p is much smaller than at $z = 0$. We thus infer that at larger distances from the window the electron heat flux is a key factor in controlling the electron temperature.

The normalized axial profiles of the Rf electric field $E_\phi^p(z)/E_\phi^p(z=0)$ in the plasma [solid, dashed, and dotted curves in Fig. 4(c)] have also been compared with the evacuated chamber case [dash-dotted curve in Fig. 4(c)]. We note that the skin length λ_s is maximal in the evacuated chamber case and can be estimated from Eq. (5) of Ref. 32. In particular, for low-frequency ICP ($\omega/c \ll 3.83/R$) operation, the skin length in the evacuated chamber can be approximated as $R/3.83$.[32] However, for large-area and higher-density discharges satisfying ($R \gg c/\omega_{pe}$), λ_s is inversely proportional to n_e [Eq. (7) of Ref. 32], which is consistent with the data in Fig. 4(c). One can also notice that, while the normalized vacuum and plasma fields are quite different, the rf field skin length in the established inductive discharge mode does not change much with power, which is a common feature of ICPs.

B. Effect of gas pressure

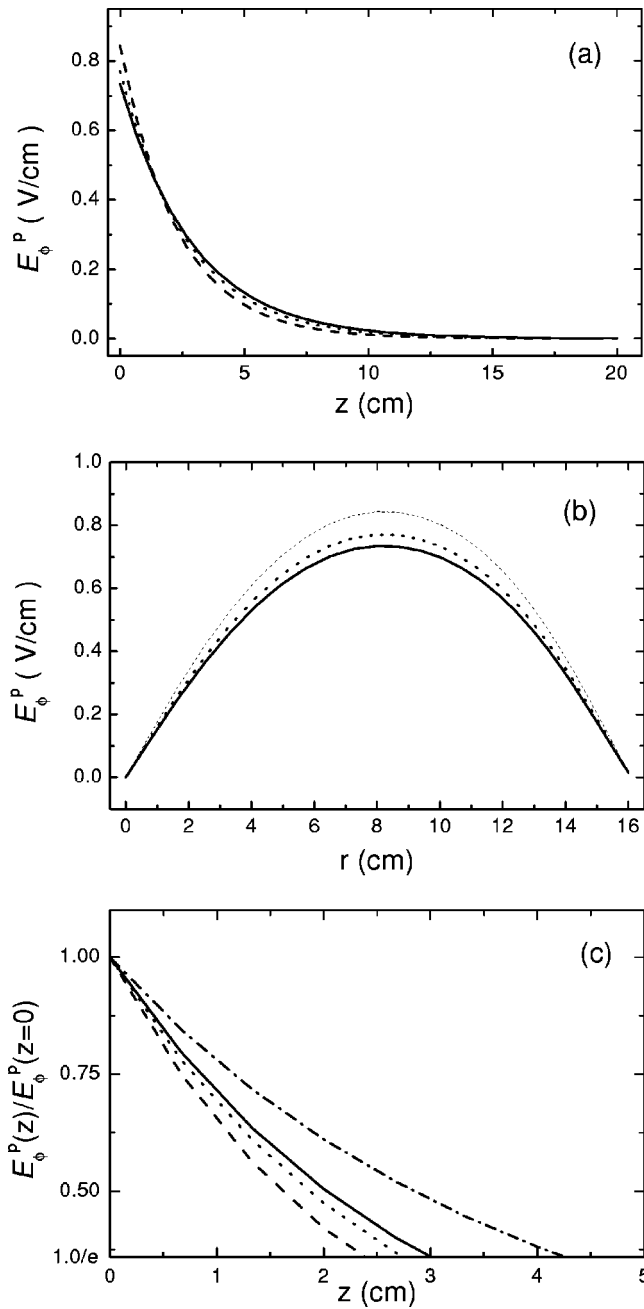We now turn to the study of the effect of the working gas pressure on the plasma parameters and power loss in the

FIG. 4. Axial (at $r=8$ cm) [(a) and (c)] and radial (at $z=0$) (b) profiles of the dimensional [(a) and (b)] and nondimensional (c) electric field E_ϕ^p for the following values of the power absorbed by the plasma $P_{in}=612.4$ W (solid curve), 771.7 W (dotted curve), and 1202.9 W (dashed curve), respectively. Dash-dotted curve in (c) corresponds to the evacuated chamber case. Other parameters are the same as in Fig. 2.

discharge. The radial profiles (at $z=6$ cm) of the electron number density and temperature computed for four different values of p_0 are presented in Figs. 5(a) and 5(b), respectively. For the same conditions as in Figs. 5(a) and 5(b) the normalized axial profiles of plasma density and electron temperature at $r=0$ are shown in Figs. 5(c) and 5(d), respectively. The plasma density in Fig. 5(c) is normalized to its value at $z=6$ cm, whereas the electron temperature is normalized to that at $z=0$.

It is clear from Fig. 5 that the working gas pressure strongly affects the plasma density and electron temperature.

We note that the Langmuir probe data suggest that within the pressure range of our interest n_e is proportional to the gas pressure for a given electron temperature. Hence, an increase of gas pressure results in elevation of the average plasma density in the plasma column and in diminishing of the electron temperature. It is also seen that the axial uniformity of the electron temperature is better at lower pressures. Furthermore, the nonuniform profiles of T_e affect the electron density distribution in the chamber [Figs. 5(a) and 5(c)]. Indeed, the density peak shifts towards the chamber top as the gas pressure rises. At $p_0=5$ mTorr the peak is close to the discharge center ($z \approx 10$ cm), which is a clear indication of the ambipolar-diffusion controlled regime at low discharge pressures. However, at $p_0=50$ mTorr the maximum of the plasma density is shifted approximately 4 cm towards the chamber top. This can indicate a possible gradual onset of a different particle loss mode, similar to what has been reported in Sec. IV A for the elevated rf powers.

The gas pressure also controls the rf power deposition process by affecting the average power loss per electron–ion pair. To elucidate the role of the electron heat flux in the plasma column we have separated the average power loss per electron θ into the collisional θ_c and heat flux θ_f components, so that $\theta = \theta_c + \theta_f$. Here

$$\theta_c = \frac{1}{\pi L R^2 \bar{n}} \int_0^R \int_0^L n(r,z) I_e(r,z) 2\pi r dr\, dz$$

and

$$\theta_f = \frac{1}{\pi L R^2 \bar{n}} \int_0^R \int_0^L \mathbf{\nabla} \cdot \mathbf{q}_e 2\pi r\, dr\, dz$$

$$= \frac{1}{\pi L R^2 \bar{n}} \int_s q_{es}\, dS,$$

where S is the total surface area of the rf discharge, and q_{es} is the component of electron flux density perpendicular to the surface.

The dependence of θ_c and θ_f on the working gas pressure are displayed in Fig. 6(a). The relative contribution of the heat transport component in the total power loss per electron $\theta_f / \theta \times 100\%$ is shown in Fig. 6(b). One can see that the heat flux contribution to the total power loss varies from 40% at low pressures ($p_0 \sim 10$ mTorr) to 17% at 100 mTorr. It should be noted that both θ_c and θ_f decline with pressure, as does the contribution of the heat flux to the total power loss per electron. The results of Fig. 6 clearly confirm the importance of the power loss through the heat flux to the chamber walls, which also strongly affects the value of the plasma density (Fig. 3).

C. Effect of the neutral gas temperature

We remark that the discharge in question is powered with relatively high rf powers. Therefore, in the plasma regions remote from the water-chilled chamber walls, areas of elevated neutral gas temperature may appear. To study the effect of the neutral gas temperature on the plasma properties, T_g was varied in computations. The radial electron density and temperature profiles calculated at $z=6$ cm, p_0
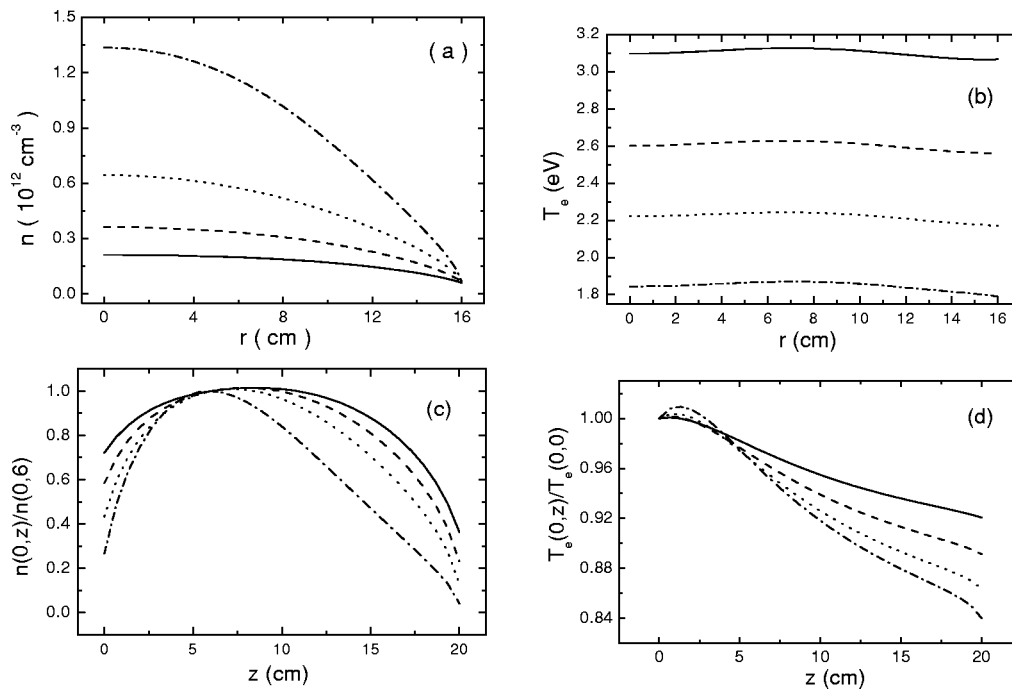
FIG. 5. Radial electron density (a) and temperature (b) profiles at $z = 6$ cm; the normalized axial density (c) and temperature (d) profiles at $r = 0$. Solid, dashed, dotted, and dash-dotted curves correspond to $p_0 = 5$, 10, 20, and 50 mTorr, respectively. Other parameters are the same as in Fig. 2.
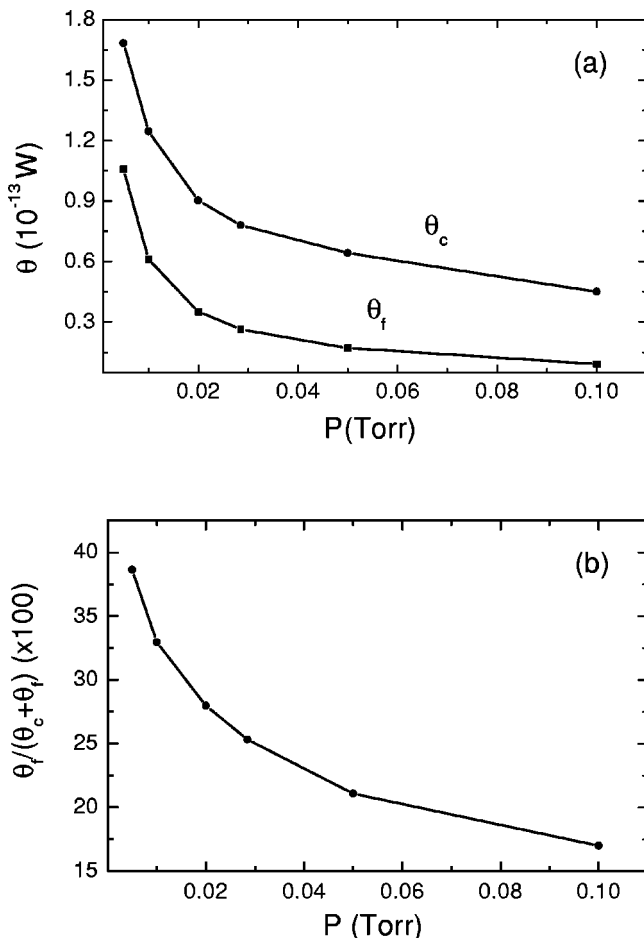

FIG. 6. Power losses into collisions θ_c and due to the electron heat flux θ_f (a), and the percentage of power lost through the electron heat flux θ_f / θ (b). The parameters are the same as in Fig. 2.

$= 28.5$ mTorr, $P_{in} = 612.4$ W for the gas temperatures $T_g = 300$, 543, and 700 K relevant to our previous plasma processing and materials synthesis experiments[15,17,18] are presented in Figs. 7(a) and 7(b). One can see from Fig. 7 that an increase of the neutral gas temperature exerts an almost similar effect on the plasma parameters as a decrease of the working gas density. This can best be understood by noting the apparent link $p_0 = n_N T_g$, which means that the fixed pressure conditions require that the neutral gas density, which enters the expressions for the most of the reaction rate coefficients, has to diminish when T_g rises.

D. Distribution of excited species

We now examine the spatial distribution of the excited argon atoms in the $3p^5 5p$ configuration. The profile of the excited atom density $n^*(r,z)$ can be calculated from[37]

$$n^*(r,z) \sim n(r,z)\nu^*(r,z), \tag{8}$$

where $\nu^*(r,z) = \nu_0^*(r,z)\exp(-U^*/T_e)$ is the excitation rate with $U^* \approx 14.5$ eV being the threshold energy for the excited level. Generally, ν_0^* is a slowly varying function of T_e.[38] Thus, evaluating $n^*(r,z)$, one can assume that ν_0^* does not depend on r and z.

The normalized profiles of the excited atoms for the two different sets of our experimental conditions are shown in Figs. 8(a) and 8(b). According to Fig. 8, the resulting spatial distributions of the excited argon species are governed by the electron density and temperature profiles. One can observe that the radial profiles of the excited atoms are hollow near the chamber top. Meanwhile, the maximum of the OEI shifts towards the chamber axis as the axial position z increases.
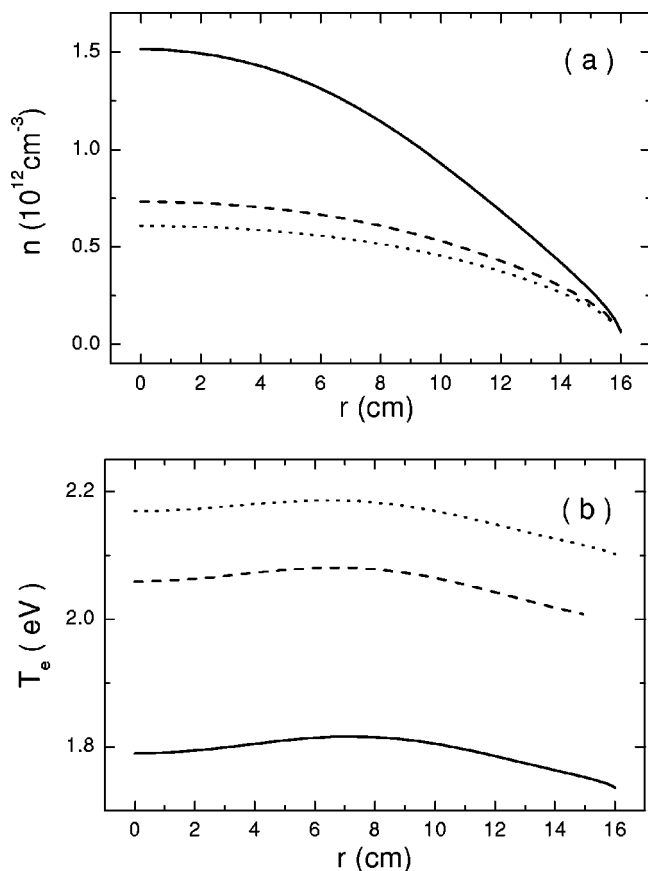
FIG. 7. Radial profiles ($z=6$ cm) of the electron density (a) and temperature (b) for different temperatures of the neutral gas T_g. Solid, dashed, and dotted curves correspond to $T_g = 300$, 543, and 700 K, respectively.

FIG. 8. Nondimensional profiles of the number density of the excited argon atoms n_{exc} in $3p^55p$ configuration at $p_0 = 29.3$ mTorr, $P_{in} = 536$ W (a) and $p_0 = 40$ mTorr, $P_{in} = 960$ W (b). In both cases $T_g = 543$ K.

Likewise, when the gas pressure grows, the ratio of $n^*(r=0)/n^*_{rmax}$ decreases, where n^*_{rmax} is the maximal density of the excited species along the radius.

We note that the radial OEI profiles have been consistently related to the integral (along the chamber axis) of the optical emission collected by the optical probe via the collimator positioned in eight portholes in the chamber bottom plate. For this purpose, the resulting local density of the excited species Eq. (8) has been integrated along z direction. Further details of the OES setup and collection of the emission can be found elsewhere.[15] The emission of the 420.07 nm argon line is due to the electron transitions from $5p$ onto $4s$ levels.[39,40] The radial distribution of emission intensity is shown in Fig. 9(a), which reveals a good consistency of the computation and experimental results. Analogously, integrating $n^*(r,z)$ in radial direction, the axial distribution of the intensity has been computed. Experimentally, the optical probe in this case was placed in seven available portholes in the side observation port of the chamber.

Figure 9(b) presents a comparison of the axial OEI profiles obtained experimentally and numerically. One can notice a remarkable agreement of the calculated emission intensities with the experimental data. However, a minor discrepancy can be seen in the radial profile in the vicinity of the discharge center. We should also note that the experiment reveals that the OEI dips ($\approx 20\%$ less than the maximal value) near the chamber axis. The computation results, cor-
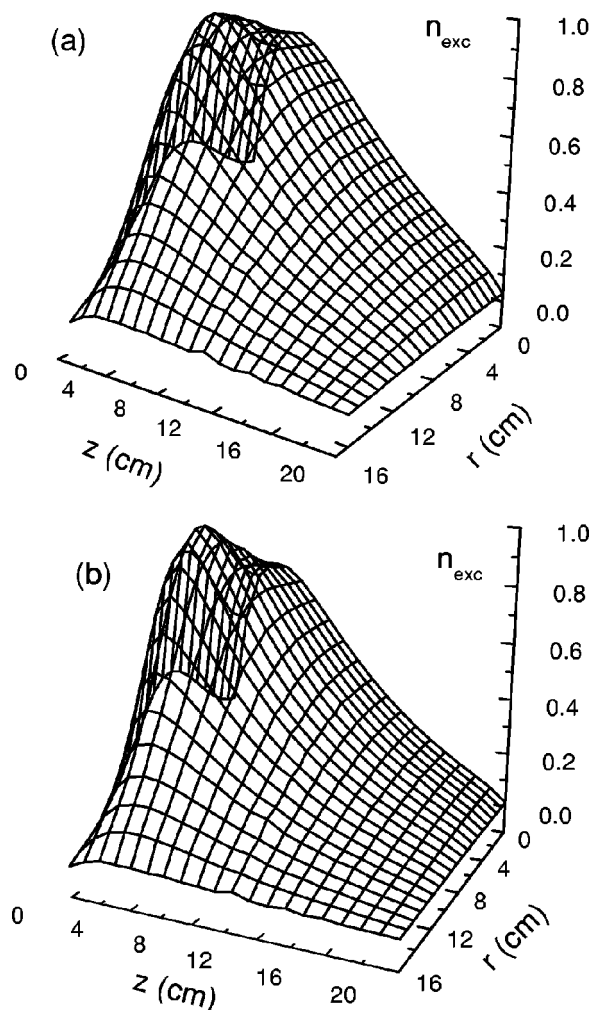
rectly following the trend, suggest less remarkable diminishing of the OEI near the chamber axis. The deviation of the computed OEIs from the experimental data is certainly within the accuracy of the model that assumes independence of ν_0^* on r and z. Further discussion on the matter can be found in the following section.

Figure 10 displays the experimental data on variation of the optical emission spectra with the operating pressure. The experiment has been carried out in the pressure range of 26–80 mTorr (argon gas flow rates were varied from 4 to 84 sccm). The intensity of the selected argon lines is presented in Fig. 11. In the pressure range concerned it is seen that there is a consistent general trend of diminishing of the OEI with p_0. For computation of the dependence OEI (p_0), the 420.07 nm line of neutral argon has been selected. This dependence has been computed for the same axial position ($z = 9.6$ cm) as in Fig. 11 and is shown in Fig. 12. In calculations, two different assumptions have been made. The first one assumes that $\nu^*(r,z) \sim n_N$ and corresponds to the dotted curve in Fig. 11. The dashed curve is obtained assuming that $\nu^*(r,z)$ does not depend on the density of neutrals. In the first case, the agreement between the theory and experiment
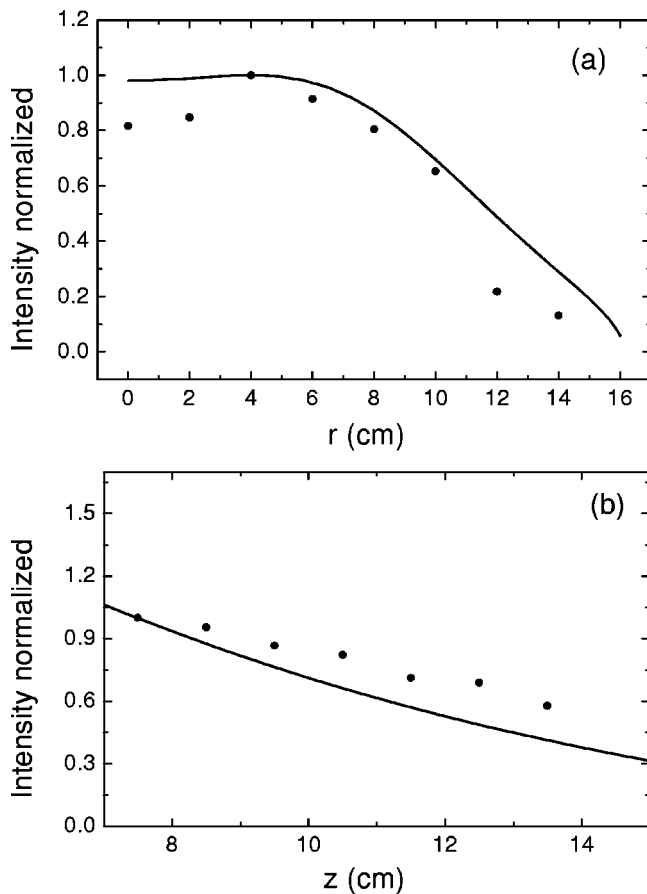
FIG. 9. The measured (dots) and computed (solid curve) radial [(a), same conditions as in Fig. 8(a)] and axial [(b), same conditions as in Fig. 8(b)] profiles of the optical emission intensity of 420.07 nm atomic argon line.

is satisfactory for the gas pressures exceeding 60 mTorr. The latter assumption provides much better consistency of the computational and experimental data within the entire range of operating pressures.

V. DISCUSSION

Here, we discuss the main results obtained and limitations of the modeling and experimental approaches. Generally, the modeling and experimental results appear to be in a good agreement, especially the data for the electron number densities [Fig. 3(a)]. However, in certain cases discrepancies of the order of few tens of percents still remain [e.g., Fig. 3(b) for the electron temperature]. It is thus worthwhile to discuss possible reasons affecting the accuracy of the simulation and experiment.

One of the possible reasons is a higher-than-expected value of the neutral gas temperature in the proximity of the Langmuir probe, causing excessive overheating of the probe tip. In this case, emissive properties of the probe surface should be carefully accounted for.[5] Although we did not systematically measure the neutral gas temperature in this set of experiments, our earlier results give an indication that, in the course of materials synthesis and processing in LF ICPs sustained with 1–2 kW rf powers, the gas temperature in the reactor chamber is maintained in the range of $T_g = 500-700$ K.[15,17,18] The above range of the neutral gas temperatures was used in most of the computations in this work. However, we do not exclude a possibility of somehow higher, than 700 K, temperatures in the area of rf power deposition. The probe tip position was, in fact, quite close to the above area, which may have resulted in less accurate values of T_g at the actual measurement position.

To verify the range of the gas temperatures in our experiments, we make a comparison with the available data from the GEC reference cell with $R = 6.5$ cm and $L = 3.1$ cm.[41] At $p_0 = 10$ mTorr, as the total input power raised from 50 to 200 W, the temperature of neutrals increased from 500 to 820 K. At fixed rf input of 200 W, $T_g = 1100$ K was achieved at $p_0 = 30$ mTorr. The estimated rf power densities W_{rf} in Ref. 41 ranged from 0.121 W/cm³ at 50 W to 0.729
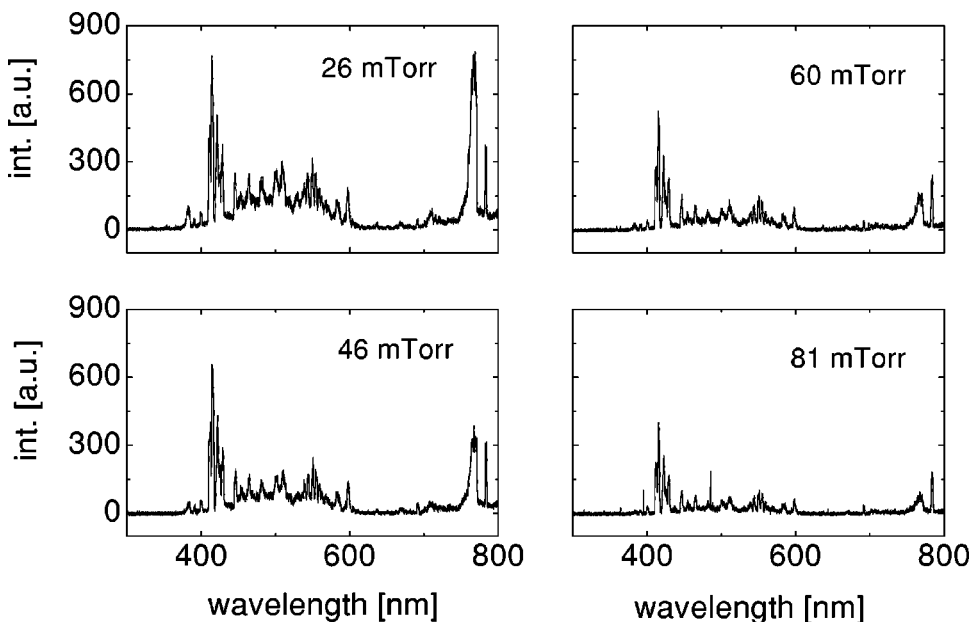

FIG. 10. Wide scan of the optical emission spectra in a discharge sustained with $P_{in} = 630$ W rf powers for different gas pressures.
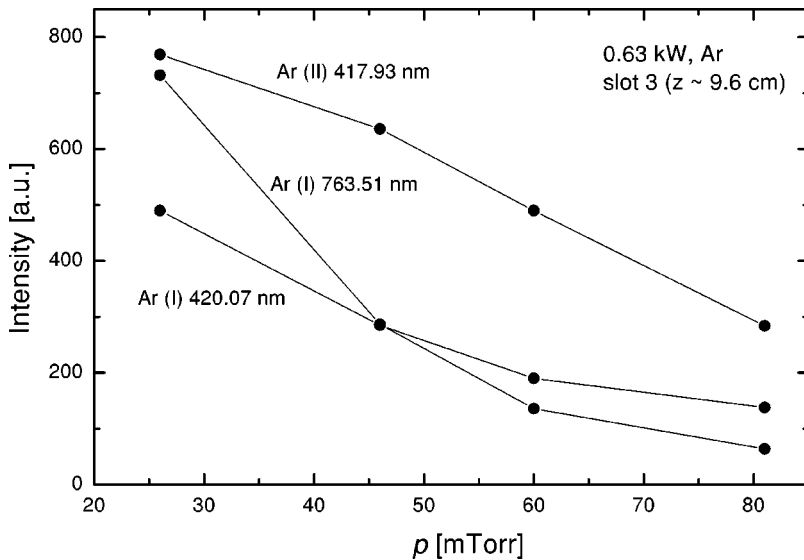
FIG. 11. OEI of selected argon lines vs pressure for $P_{in} = 630$ W. The position of the optical probe is $z = 9.6$ cm.

W/cm^3 at 300 W. In our experiments with the much larger chamber, variation of the input power from 600 to 1700 W reflected changes in W_{rf} from 0.037 to 0.105 W/cm^3. Thus, comparison of the neutral gas temperatures at similar rf power densities (although at quite different experimental conditions including gas pressure) does confirm the reasonability of our results on T_g in the processing chamber.

The other limitation of the modeling effort in this work is the apparent inaccuracy in the excitation/ionization rate coefficients calculated for Maxwellian EEDFs. Indeed, as our experimental measurements of the EEDF suggest (Fig. 13), the latter is not necessary is the case. Figure 13 presents the variation of the EEDF with input power [Fig. 13(a)] and comparison with the corresponding Maxwellian EEDF plotted using the same values of the electron number density and temperature as in the experiment [Fig. 13(b)]. One can see from Fig. 13(a) that the total area under the EEDF increases with rf power, which obviously confirms proportionality of the electron/ion number densities to the power absorbed by

the plasma column.[5] However, the power does not noticeably affect the shape of the curve. The EEDF maximum is slowly shifting towards higher values of the electron energy while P_{in} increases. From Fig. 13(b) one can clearly observe that the measured EEDF is somehow different from the corresponding Maxwellian one. Specifically, the peak of the measured EEDF is higher and corresponds to larger values of the electron energy. On the other hand, the Maxwellian EEDF gives a larger number of high-energy electrons, with the energies exceeding 13–14 eV. From Fig. 13 one can notice that the measured EEDF has a shape similar to the Maxwellian shape, with the peak shifted toward higher values of the energy, which is peculiar to Dryuvestein-like EEDFs.[5] A possible factor that affects a remarkable deviation of the experimentally measured EEDF from a Maxwellian one is strong electric fields in the rf power deposition area. Also, notable divergence of EEDFs from Maxwellian ones in the skin layer of low frequency ICPs can be attributed to the ponderomotive effect.[16]
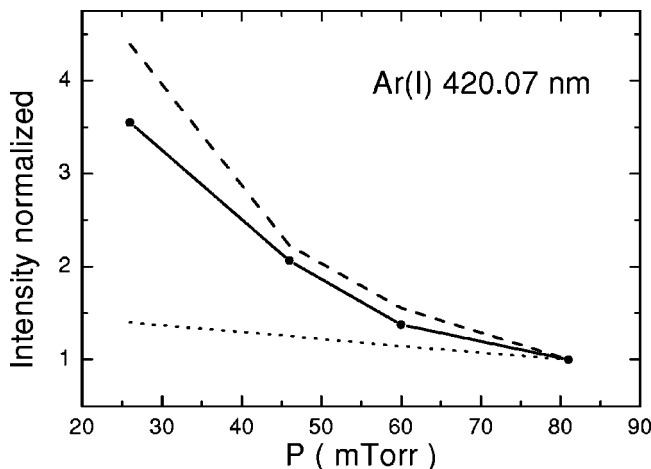

FIG. 12. Nondimensional optical emission intensity of Ar(I) 420.07 nm line (normalized on its value at $p_0 = 81$ mTorr). Other parameters are the same as in Fig. 11. The solid, dashed, and dotted curves correspond to the experiment, calculations with $\nu^*(n_N) =$ const and $\nu^* \sim n_N$, respectively.
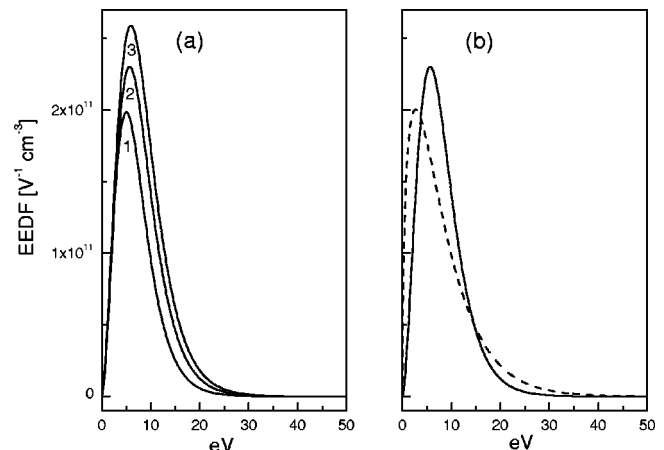

FIG. 13. The measured ($r = 4$ cm, $z = 5.6$ cm) EEDFs for different rf powers at $p_0 = 28.9$ mTorr. Curves 1–3 are plotted for $P_{in} = 612$, 919, and 1203 W, respectively. Comparison of the measured (solid curve) EEDF with the Maxwellian (dashed curve) one ($P_{in} = 919$ W).

It is notable that the electrons with higher energies play an important role in nonelastic electron-impact processes. Thus, the depletion of the electron number density should be accompanied by a decrease of the excitation and ionization rates, which inevitably results in a growth of the electron temperature should the gas pressure remain the same.

Another factor affecting relatively higher values of the measured electron temperature is a lower than conventional frequency of the rf generator. At 30 mTorr, the rate of the electron–neutral collisions is much larger the rf frequency ($\nu_{en} \gg \omega$). Hence, the electrons receive the energy from the rf field as if they are in a dc electric field, acquiring somehow higher thermal energy.

Furthermore, the electron–electron collision rate ν_{ee} may not necessarily be large enough to "Maxwellize" the EEDF. It can be estimated as $\nu_{ee} \sim n_e \sigma_{ee}\sqrt{T_e/m_e}$, where n_e is the electron number density, T_e is the electron temperature, and $\sigma_{ee} \sim 2.9 \times 10^{-13} T_e^{-2}$ cm^2[38] is the cross section of electron–electron collisions. For $n_e \gtrsim 5.0 \times 10^{11}$ cm^{-3} and $T_e \sim 2$ eV, $\nu_{ee} \gtrsim 10^6$ s^{-1}, which is the value of the same order of magnitude as the rates of inelastic collisions.[33]

Meanwhile, the mean free path of electrons becomes larger at lower pressures. Hence, some part of the electron population receiving the energy from the rf electric field near the chamber top can affect the EEDF non-locally. In this case the solution of a nonuniform Boltzmann equation is required to obtain viable values of the plasma parameters. Finally, the discrepancy between the experiment and computation can certainly be attributed to the experimental uncertainties in the Langmuir probe signal acquisition and measurement techniques.

We emphasize that the best agreement between the computed and measured values of the plasma density [Fig. 3(a)] has been achieved in case of taking into account the heat flux onto the chamber walls ($\nabla T_e \neq 0$). For nonvanishing heat flux boundary conditions, at $P_{in} < 800$ W the numerically obtained value of the plasma density is almost the same as the experimental one. As the power increases ($P_{in} > 800$ W) the calculated plasma density becomes larger than the one obtained in experiment. The discrepancy can be attributed to the observed increase of T_e in the subsequent power range [Fig. 3(b)]. Accordingly, the elevated electron temperature forces the plasma density to decrease should W_{rf} remain the same.

The electron number density calculated in case of the vanishing heat flux onto the chamber walls ($\nabla T_e = 0$) appears to be 20%–30% larger when the one obtained assuming $\nabla T_e \neq 0$. It is consistent with the results of Fig. 6 suggesting that under prevailing experimental conditions the electron heat fluxes consume up to 20%–30% of the total power. Thus, not accounting for such a significant power loss channel results in higher, than in the experiment, values of n_e.

The remarkable agreement between the experimental and numerical (dashed) curves in Fig. 12 suggests that when the OEI declines with the gas pressure, it is likely that the excitation rate $\nu^*(r,z)$ indeed does not depend on the density of neutrals. Thus, we can presume that the increase of the working gas pressure results in pronounced elevation of

T_g. This tendency is consistent with the available experimental data.[42]

Finally, knowledge on the neutral gas temperature and heat fluxes in plasma processing discharges is becoming a matter of outmost importance for a number of applications. In particular, recent results on growth of nanostructured silicon-based films have convincingly demonstrated the neutral gas temperature as a critical factor in management of hydrogenated silicon nanoparticles in γ (powder-generating) regime.[43]

VI. CONCLUSIONS

Results on the diagnostics and numerical modeling of low-frequency ($\sim$460 kHz) inductively coupled plasmas are presented in this article. Comparisons are made between the experimental and numerical data, particularly for the electron density and temperature, which show reasonable agreement. Possible reasons for any discrepancies are discussed. A study of the influence of the gas pressure and temperature on plasma density and electron temperature shows that an increase of working gas temperature has the same effect as a decrease of gas pressure. The electron heat flux to the walls appears to be a factor in the total rf power loss, as is also the neutral gas pressure. Measurements were made of the spatial distribution of the optical emission intensities of the excited argon species in both radial and axial directions. These show good agreement with the calculated emission intensities.

The fairly accurate agreement between the numerical and experimental results confirms the viability of the 2D fluid discharge model in simulating the major parameters of low frequency inductively coupled plasmas. The model can further be improved by involving both local and nonlocal kinetic approaches, stepwise excitation and ionization processes, complex gas chemistries including radicals, molecular complexes, and negative ions, details of the process (e.g., substrate bias, power and mass transport in near-substrate areas), as well as the effects of the near-wall sheath/presheath areas.

ACKNOWLEDGMENTS

[1] F. F. Chen, Phys. Plasmas **2**, 2164 (1995).
[2] H. Sugai, T. H. Ahn, I. Ghanashev, M. Goto, M. Nagatsu, K. Nakamura, K. Suzuki, and H. Toyoda, Plasma Phys. Controlled Fusion **39**, A445 (1997).
[3] H. Sugai, I. Ghanashev, M. Hosokawa, K. Mizuno, K. Nakamura, H. Toyoda, and K. Yamauchi, Plasma Sources Sci. Technol. **10**, 378 (2001).
[4] M. A. Lieberman and R. A. Gottscho, in *Physics of Thin Films*, edited by M. Francombe and J. Vossen (Academic, New York, 1993).
[5] M. A. Lieberman and A. J. Lichtenberg, *Principles of Plasma Discharges and Materials Processing* (Wiley, New York, 1994).
[6] J. Hopwood, Plasma Sources Sci. Technol. **1**, 109 (1992); J. H. Keller, Plasma Phys. Controlled Fusion **39**, A437 (1997).

[7] H. Sugai, K. Nakamura, and K. Suzuki, Jpn. J. Appl. Phys., Part 1 **33**, 2189 (1994).

[8] K. Suzuki, K. Nakamura, H. Ohkubo, and H. Sugai, Plasma Sources Sci. Technol. **7**, 13 (1998).

[9] M. Tuszewski, Phys. Plasmas **5**, 1198 (1998).

[10] M. Tuszewski, IEEE Trans. Plasma Sci. **27**, 68 (1999).

[11] I. M. El-Fayoumi and I. R. Jones, Plasma Sources Sci. Technol. **7**, 162 (1998).

[12] S. Xu, K. N. Ostrikov, W. Luo, and S. Lee, J. Vac. Sci. Technol. A **18**, 2185 (2000).

[13] K. N. Ostrikov, S. Xu, and M. Y. Yu, J. Appl. Phys. **88**, 2268 (2000).

[14] S. Xu, K. N. Ostrikov, Y. Li, E. L. Tsakadze, and I. R. Jones, Phys. Plasmas **8**, 2549 (2001).

[15] K. N. Ostrikov, S. Xu, and A. B. M. Shafiul Azam, J. Vac. Sci. Technol. A **20**, 251 (2002).

[16] V. A. Godyak, B. M. Alexandrovich, and V. I. Kolobov, Phys. Rev. E **64**, 026406 (2001).

[17] E. L. Tsakadze, K. N. Ostrikov, N. Jiang, R. Ahmad, and S. Xu, Int. J. Mod. Phys. B **16**, 1143 (2002).

[18] N. Jiang, S. Xu, K. N. Ostrikov, J. D. Long, J. W. Cai, and Z. L. Tsakadze, Int. J. Mod. Phys. B **16**, 1132 (2002).

[19] H. M. Wu, B. W. Yu, A. Krishnan, M. Li, Y. Yang, J. P. Yan, and D. P. Yuan, IEEE Trans. Plasma Sci. **25**, 776 (1997).

[20] R. A. Stewart, P. Vitello, D. B. Graves, E. F. Jaeger, and L. A. Berry, Plasma Sources Sci. Technol. **4**, 36 (1995).

[21] C. M. Ryu and M. Y. Yu, Phys. Scr. **57**, 601 (1998).

[22] M. Y. Yu and L. Stenflo, Nature (London) **384**, 224 (1996).

[23] N. F. Cramer, J. Phys. D **30**, 2573 (1997); T. A. van der Straaten, N. F. Cramer, I. S. Falconer, and B. W. James, *ibid.* **31**, 191 (1998).

[24] S. V. Vladimirov, S. A. Maiorov, and N. F. Cramer, Phys. Rev. E **63**, 045401 (2001).

[25] M. M. Turner, Phys. Rev. Lett. **71**, 1844 (1993).

[26] H. M. Wu, Plasma Sources Sci. Technol. **9**, 347 (2000).

[27] U. Kortshagen, C. Busch, and L. D. Tsendin, Plasma Sources Sci. Technol. **5**, 1 (1996).

[28] S. A. Maiorov, S. V. Vladimirov, and N. F. Cramer, Phys. Rev. E **63**, 017401 (2001).

[29] D. B. Hash, D. Bose, M. V. V. S. Rao, B. A. Cruden, M. Meyyappan, and S. P. Sharma, J. Appl. Phys. **90**, 2148 (2001).

[30] J. Henriques, E. Tatarova, F. M. Dias, and C. M. Ferreira, J. Appl. Phys. **90**, 4921 (2001).

[31] H. Sugai, I. Ghanashev, and M. Nagatsu, Plasma Sources Sci. Technol. **7**, 192 (1998).

[32] V. Vahedi, M. A. Lieberman, G. DiPeso, T. D. Rognlien, and D. Hewett, J. Appl. Phys. **78**, 1446 (1995).

[33] V. E. Golant, A. P. Zhilinskii, and I. E. Sakharov *Fundamentals of Plasma Physics* (Wiley, New York, 1980).

[34] S. Ashida, C. Lee, and M. A. Lieberman, J. Vac. Sci. Technol. A **13**, 2498 (1995).

[35] N. A. Azarenkov, I. B. Denysenko, A. V. Gapon, and T. W. Johnston, Phys. Plasmas **8**, 1467 (2001).

[36] I. B. Denysenko, A. V. Gapon, N. A. Azarenkov, K. N. Ostrikov, and M. Y. Yu, Phys. Rev. E **65**, 046419 (2002).

[37] I. Peres, M. Fortin, and J. Margot, Phys. Plasmas **3**, 1754 (1996).

[38] L. M. Biberman, V. S. Vorob'ev, and I. T. Yakubov, *Kinetics of Non-equilibrium Low-Temperature Plasma* (Nauka, Moscow, 1982) (in Russian).

[39] D. R. Lide, *CRC Handbook on Chemistry and Physics*, 78th ed. (Chemical Rubber Corp., New York, 1997).

[40] C. M. Ferreira and J. Loureiro, Plasma Sources Sci. Technol. **9**, 528 (2000).

[41] G. A. Hebner, J. Appl. Phys. **80**, 2624 (1996).

[42] V. Lisovsky (private communication).

[43] A. Hadjadj, L. Boufendi, S. Huet, S. Schelz, P. Roca i Cabarrocas, H. Estrade-Szwarckopf, and B. Rousseau, J. Vac. Sci. Technol. A **18**, 529 (2000).